The Astrophysical Journal, 894:111 (16pp), 2020 May 10 https://doi.org/10.3847/1538-4357/ab86a2

Disentangling Dust Components in SN 2010jl: The First 1400 Days

A. M. Bevan[1], K. Krafton[2], R. Wesson[1], J. E. Andrews[3], E. Montiel[4], M. Niculescu-Duvaz[1], M. J. Barlow[1], I. De Looze[5], and G. C. Clayton[2]
[1] Department of Physics and Astronomy, University College London, Gower Street, London WC1E 6BT, UK; antonia.bevan.12@ucl.ac.uk
[2] Department of Physics & Astronomy, Louisiana State University, Baton Rouge, LA 70803, USA
[3] Steward Observatory, University of Arizona, 933 North Cherry Avenue, Tucson, AZ 85721, USA
[4] SOFIA-USRA, NASA Ames Research Center, MS 232-12, Moffett Field, CA 94035, USA
[5] Department of Physics and Astronomy, Ghent University, Krijgslaan 281, S9, B-9000 Gent, Belgium
Received 2019 November 25; revised 2020 March 25; accepted 2020 March 26; published 2020 May 12

Abstract

The luminous Type IIn SN 2010jl shows strong signs of interaction between the SN ejecta and dense circumstellar material. Dust may be present in the unshocked ejecta; the cool, dense shell (CDS) between the shocks in the interaction region; or in the circumstellar medium (CSM). We present and model new optical and infrared photometry and spectroscopy of SN 2010jl from 82 to 1367 days since explosion. We evaluate the photometric and spectroscopic evolution using the radiative transfer codes MOCASSIN and DAMOCLES, respectively. We propose an interaction scenario and investigate the resulting dust formation scenarios and dust masses. We find that SN 2010jl has been continuously forming dust based on the evolution of its infrared emission and optical spectra. There is evidence for preexisting dust in the CSM as well as new dust formation in the CDS and/or ejecta. We estimate that 0.005–0.01 $M_{\odot}$ of predominantly carbon dust grains has formed in SN 2010jl by ∼1400 days post-outburst.

Unified Astronomy Thesaurus concepts: Core-collapse supernovae (304); Type II supernovae (1731); Circumstellar dust (236); Dust continuum emission (412); Dust nebulae (413); Astronomical models (86); Radiative transfer (1335); Extinction (505); Circumstellar shells (242); Dust shells (414)

Supporting material: data behind figure

1. Introduction

Dust evolution in Type IIn supernovae (SNe) is complex. Noninteracting SNe generally begin forming dust in their cooling ejecta several hundred days post-outburst (e.g., Sugerman et al. 2006; Bevan et al. 2017; Matsuura et al. 2017). However, in an SN IIn, the interaction between the forward shock and the surrounding dense circumstellar medium (CSM) at much earlier times propagates a reverse shock back into the ejecta, complicating this picture. Between the two shocks is a rapidly cooling region, the cool, dense shell (CDS), where new grains of dust may be able to condense (Pozzo et al. 2004). Dust grains may still be able to condense in the unshocked ejecta, and preexisting dust that formed during pre-SN mass-loss phases may also be present in the CSM. Disentangling the contributions of each of these dust components to the observable signatures of interacting SNe is important for understanding the evolution of dust in interacting SNe as well as for interpreting their observations.

The bright Type IIn SN 2010jl is an interesting laboratory for the study of dust formation, evolution, and destruction. SN 2010jl was discovered on 2010 November 3.52 in the irregular galaxy UGC 5189A at a distance of 48.9 ± 3.4 Mpc (Newton & Puckett 2010) and, following its discovery, has been well observed. With a peak absolute magnitude of ∼−20, this was one of the brightest SNe in recent years (Stoll et al. 2011). Early spectra of its broad emission features near maximum light showed narrow-line emission, leading to SN 2010jl's classification as an SN IIn (Benetti et al. 2010; Yamanaka et al. 2010). SN 2010jl's interaction with a dense CSM allowed it to be detected in X-rays (Immler et al. 2010), and it is among the most luminous X-ray SNe yet observed (Chandra et al. 2012).

The often long-lasting circumstellar interaction of SNe IIn results in significantly more complex geometry than noninteracting SNe. Generally, interacting SNe are assumed to consist of concentric shells of unshocked ejecta, reverse-shocked ejecta adjoining forward-shocked CSM with a CDS of material at their boundary, and unshocked CSM outside of the forward shock. Diagrams illustrating this scenario are abundant in the literature (see, e.g., Chevalier & Fransson 1994; Smith 2017; Sarangi et al. 2018). The characteristic narrow-line emission seen in SNe IIn arises in the flash-ionized CSM. In the case of SN 2010jl, there are numerous narrow optical emission features. In most cases, these displayed a P-Cygni profile for the first few hundred days, indicative of high densities in the line-emitting region of the CSM (Fransson et al. 2014). Preexisting dust may be present in the unshocked CSM that formed in pre-SN outbursts or winds. The presence of an IR excess throughout the first ∼400 days of the evolution of SN 2010jl has been attributed to a light echo caused by such preexisting, circumstellar dust (Kilic et al. 2011; Fransson et al. 2014).

In addition to preexisting, circumstellar dust, SN 2010jl exhibits signatures of newly formed dust associated with the interacting system. New dust formation inside core-collapse SNe (CCSNe) can give rise to three observable signatures: (1) an IR excess due to thermal emission from hot or warm dust, (2) a concurrent increased rate of fading of the optical flux, and (3) a progressive and systematic blueshift of emission-line profiles as the receding parts of the expanding SN are increasingly blocked by new dust. The IR excess can also be caused by preexisting circumstellar dust heated by the UV flash, but preexisting dust likely only makes a significant contribution to the IR excess at early times because it fades rapidly for most geometries. SN 2010jl exhibited an IR excess at early and later stages along with blueshifted line profiles, leading a number of authors to infer the formation of new dust in its CDS and/or in its ejecta (e.g., Andrews et al. 2011;

Table 1
BVRI Photometry of SN 2010jl from Gemini/GMOS-S

Date	JD	Age (days)	V (mag)	R (mag)	I (mag)
2012 Mar 19	2456006	526	17.26 ± 0.05	16.43 ± 0.05	16.83 ± 0.02
2012 May 17	2456065	585	17.60 ± 0.06	16.79 ± 0.02	17.28 ± 0.03
2013 Feb 10	2456334	854	19.01 ± 0.08	18.44 ± 0.05	18.74 ± 0.07
2013 Apr 12	2456395	915	19.33 ± 0.08	19.03 ± 0.05	19.27 ± 0.07
2014 Apr 18	2456766	1286	21.24 ± 0.06	19.79 ± 0.03	20.93 ± 0.05

Smith et al. 2012; Maeda et al. 2013; Fransson et al. 2014; Gall et al. 2014; Chugai 2018; Sarangi et al. 2018).

In this paper, we have determined the evolution of dust in SN 2010jl over the first 1400 days. We have further sought to disentangle preexisting dust in the unshocked CSM from newly formed dust behind the SN shock front. We have obtained new visible and IR photometry and spectroscopy using Gemini/GMOS and Spitzer/IRAC during the first 1400 days of SN 2010jl's evolution, which we have supplemented with data from online archives. We have built a careful model of SN 2010jl based on these data and have applied two 3D Monte Carlo radiative transfer codes (MOCASSIN and DAMOCLES) to simultaneously model the spectral energy distributions (SEDs) and asymmetric dust-affected emission-line profiles at a range of epochs in order to distinguish between different dust populations in SN 2010jl and to determine their respective dust masses.

This paper is organized as follows. In Section 2, we describe the optical and infrared photometry and optical spectroscopy obtained with the Gemini North and South telescopes, the Spitzer Space Telescope, and the European Southern Observatory's Very Large Telescope and New Technology Telescope (ESO/VLT/NTT). In Section 3, we discuss observational signatures of dust in SN 2010jl before presenting our DAMOCLES modeling of red–blue asymmetries in the optical emission lines and MOCASSIN modeling of optical–IR SEDs in Section 4. In Section 5, we present a discussion of our results before summarizing in Section 6.

2. Observations

The first detection of SN 2010jl was from prediscovery images obtained on 2010 October 9.6 (Stoll et al. 2011). For this paper, we adopt an explosion date of 2010 October 10.

2.1. Photometry

New images and spectra of SN 2010jl were obtained over five epochs with Gemini/GMOS-S (GS-2012A-Q-79, GS-2013A-Q-93, GS-2014A-Q-70, GN-2016A-Q-85-31). The g' r' i' images were reduced and stacked using the IRAF gemini package (Tody 1986, 1993). The instrumental g' r' i' magnitudes were transformed to standard Johnson–Cousins *VRI* using the tertiary standards presented in Andrews et al. (2011) and transformations presented in Welch et al. (2007). Uncertainties were calculated by adding in quadrature using the transformation uncertainty quoted in Welch et al. (2007), photon statistics, and the zero-point deviation of the standard stars for each epoch. The derived *VRI* magnitudes are provided in Table 1. Differences between our *VRI* magnitudes and those presented by Fransson et al. (2014) may be due to their corrections to account for line emission. We did not apply any such corrections to our data as, except for the *R* band, we do not find that line emission significantly contributes to the broadband fluxes.

Spitzer/IRAC (3.6 and 4.5 μm) images of SN 2010jl were obtained at six epochs during 2011–2014. A further five epochs during this period were taken from the Spitzer Heritage Archive[6] (Fox et al. 2013; Szalai et al. 2019), along with the pipeline basic calibrated data. Preexplosion IRAC images of UGC 5189A, available in the Spitzer archive from 2007 December 27 (Program 40301, PI Fazio), were used to subtract the host galaxy from the SN 2010jl images to allow for more accurate photometry. Aperture photometry was performed using standard IRAF routines (digiphot/apphot/phot). Eight IRAC observations were obtained with frametimes of 100 s and three of 30 s. Some of the 100 s integrations suffer from saturation effects in some pixels. However, at three epochs (253, 993, and 1367 days), unsaturated observations with 30 s exposures were also obtained within a few days of the 100 s observations. The 30 s exposures were used to correct the fluxes of the 100 s observations for the saturation effects. The 30 and 100 s exposures taken on days 253 and 260, respectively, showed only a 2% difference in the count rates, which we considered to be negligible. At days 993 and 997, however, the 30 s exposure had a significantly higher count rate than the 100 s exposure in both bands, by 38% in the 3.6 μm band and 31% in the 4.5 μm band. On days 1367–8, the 30 s exposure was brighter than two 100 s exposures in both bands, by 13% in the 3.6 μm band and 12% in the 4.5 μm band.

The 100 s exposures taken on days 464, 620 and 843 did not have 30 s exposures taken at similar times. These observations were only partially saturated, and we therefore conservatively corrected the flux at these epochs using the 38% (31%) difference between the different frametimes in the 3.5 μm (4.6 μm) band at 993 days as a correction factor. We show the saturated fluxes of 8.55 mJy (3.6 μm) and 8.30 mJy (4.5 μm) as a lower limit on our plots in Section 4.3.

The optical and IR light curves are shown in Figure 1. Table 2 lists the Spitzer fluxes and their 1σ uncertainties for the seven epochs used for the analysis in this paper. The 100 s observations used to establish the saturation correction are not included in Table 2. We estimate that the uncertainty in the saturation correction for individual epochs is ∼10%. These uncertainties were combined with the photometric uncertainties. They are listed in Table 2.

*JHK*s imaging obtained with NTT/SOFI (184.D-1151, PI Benetti) at La Silla was retrieved from the ESO Science Archive Facility. Reductions were done using the standard procedure in IRAF, including crosstalk and flatfield correction, background subtraction, and the shifting and adding of individual image frames. Aperture photometry was then done using a set of standard stars in the field obtained from the Two

[6] https://sha.ipac.caltech.edu/applications/Spitzer/SHA/

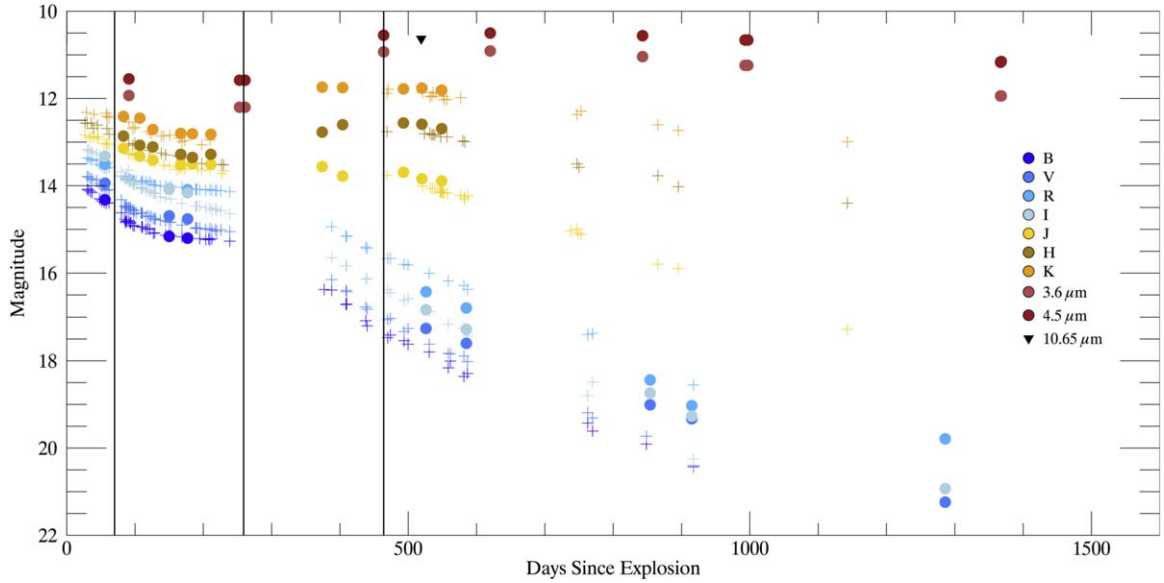

Figure 1. Optical and IR light curves of SN 2010jl. Circles represent data from Andrews et al. (2011) and new data presented in Tables 1–2 in this paper. Crosses represent data from Fransson et al. (2014). The vertical lines represent different landmarks of SN 2010jl's evolution. The first line, at about Day 70, marks a transition in SN 2010jl's spectra. Before this time, the spectra do not have IWCs in any lines. After the first vertical line, IWCs arise in the Balmer and He I λ 5876 Å lines and begin to shift to the blue. This is also when the initial IR excess emerges. The second vertical line marks the beginning of a gap in the observations. From the second line to the third line, there is a sharp rise in the IR fluxes, and the IWCs' blueshifts continue to strengthen. After the third line, we continue to see evidence of dust formation via an IR excess and blueshifted optical line profiles.

Table 2
Spitzer/IRAC Photometry of SN 2010jl

Date	JD	Age (days)	3.6 μm (mJy)	4.5 μm (mJy)
2011 Jan 9	2455571	91	4.14 ± 0.11	4.32 ± 0.12
2011 Jun 20	2455732	253	3.68 ± 0.10	4.18 ± 0.12
2012 Jan 17[a]	2455944	464	11.75 ± 0.31	10.84 ± 0.27
2012 Jun 21[a]	2456100	620	12.04 ± 0.32	11.35 ± 0.27
2013 Jan 30[a]	2456323	843	10.62 ± 0.25	10.69 ± 0.25
2013 Jun 29	2456472	993	8.81 ± 0.09	9.81 ± 0.10
2014 Jul 8	2456846	1367	4.67 ± 0.12	6.09 ± 0.16

Note.
[a] Integrations of 100 s corrected for saturation effects.

Micron All Sky Survey catalog. The *JHK*s photometry is presented in Table 3.

We observed SN 2010jl with VLT/VISIR on 2012 March 12 (day 519), using the B10.7 filter (10.7 μm; ESO program 288.D-5044(A)). The standard VISIR pipeline recipes were used with ESOREX, and flux calibration was done using a standard star observed immediately after the target at similar airmass. The SN was not detected in this observation; from the rms variations in the reduced image, we estimated a 3σ upper limit of 2 mJy for the 10.7 μm flux density.

The extinction from the Milky Way along the line of sight to SN 2010jl is very small, $E(B-V) = 0.027$ (Schlegel et al. 1998). The flux measurements are corrected for this Galactic foreground extinction, assuming $R_V = 3.1$ (Cardelli et al. 1989). There is evidence for a small amount of additional reddening ($E(B-V) \sim 0.03$) from dust associated with the host galaxy, from the equivalent width measured for a Na I D_2 component at the velocity of UGC 5189A (Patat et al. 2011).

Using our new observations as well as data from the literature (Andrews et al. 2011; Fransson et al. 2014), we present optical (*BVRI*) and IR (*JHK*s, 3.6, 4.5 μm) light curves extending out to almost 1400 days in Figure 1.

2.2. Spectroscopy

For each Gemini/GMOS epoch (526, 585, 854, 915 and 1286 days), spectra were obtained from three 900 s exposures taken in longslit mode using the B600 grating and a slit width of 0.″75. Central wavelengths of 5950, 5970, and 5990 Å were chosen ensure complete spectral coverage accounting for chip gaps. A 2 × 2 binning in the low-gain setting was used. As with the imaging, the spectra were reduced using the IRAF gemini package. The sky subtraction regions were determined by visual inspection to prevent contamination from material not associated with the SN, and the spectra were extracted using 15 rows centered on the SN. We also made use of day 34–247 ESO archival VLT X-Shooter spectra that were originally presented by Gall et al. (2014). The spectra from each individual night have been corrected for the radial velocity of UGC 5189A (3167 km s^{-1}). The spectra and the evolution of the line profiles are presented in Figures 2 and 3.

3. Observational Signatures of Dust in SN 2010jl

3.1. The IR Excess

The IR excess, apparent by day 91, persists through all our epochs of observations to day 1367 (Figure 1). Previous models by Andrews et al. (2011) and Fransson et al. (2014) have suggested that the IR-excess emission at early times is likely dominated by an IR echo caused by the flash heating of preexisting dust in the CSM. At later times, however, it is unlikely that the echo could sustain the observed IR excess (see Section 4.3). This points toward a transition in the dominating dust emission component from preexisting echoing dust in the CSM to warm or hot newly formed dust in the CDS or ejecta. The near-IR jumps in brightness between days 260 and 464 at

Table 3
JHKs Photometry of SN 2010jl from NTT/SOFI

Date	JD	Age (days)	J (mag)	H (mag)	K_s (mag)
2011 Jan 1	2455562	83	13.10 ± 0.05	12.75 ± 0.12	12.35 ± 0.08
2011 Jan 25	2455587	107	13.25 ± 0.01	13.01 ± 0.02	12.46 ± 0.11
2011 Feb 13	2455606	126	13.30 ± 0.04	13.04 ± 0.05	12.65 ± 0.12
2011 Mar 26	2455647	167	13.46 ± 0.03	13.21 ± 0.05	12.75 ± 0.07
2011 Apr 12	2455664	184	13.43 ± 0.06	13.25 ± 0.10	12.85 ± 0.10
2011 May 9	2455691	211	13.40 ± 0.18	13.16 ± 0.09	12.88 ± 0.12
2011 Jun 25	2455738	258	13.48 ± 0.07	13.25 ± 0.08	12.73 ± 0.11
2011 Oct 19	2455853	374	13.59 ± 0.10	12.77 ± 0.10	11.67 ± 0.10
2011 Nov 18	2455883	404	13.46 ± 0.04	12.60 ± 0.14	11.72 ± 0.13
2012 Feb 15	2455972	493	13.74 ± 0.02	12.58 ± 0.07	11.78 ± 0.12
2012 Mar 13	2455999	520	13.88 ± 0.06	12.64 ± 0.09	11.74 ± 0.10
2012 Apr 11	2456028	549	13.91 ± 0.04	12.74 ± 0.04	11.85 ± 0.08

both 3.6 and 4.5 μm before slowly declining over a period of nearly 1000 days. The H and K bands also brighten substantially during this time, ∼1 yr post-outburst, before steadily declining. The sudden increase in IR flux between days 260 and 464 is a strong indicator of new dust formation. Concurrently, the rate of decline of the optical bands increases significantly. However, it is not possible to attribute this accelerated decline definitively to dust formation due to the lack of data between ∼200 and 350 days. Conversely, the lack of a wavelength dependence in the rate of decline in the visible bands does not necessarily preclude dust formation being the cause because larger dust grain sizes, as have been inferred to have formed in other CCSNe (Wesson et al. 2015; Bevan et al. 2017), could reduce the wavelength dependence of extinction in the optical.

3.2. Asymmetric Emission-line Profiles

In order to interpret and model the effects of dust on the emission-line profiles of SN 2010jl, we must first consider the different emitting components that contribute to line profiles of interacting SNe. SNe IIn are identified by narrow emission lines ∼100 km s^{-1} in width which arise in the flash-ionized, unshocked CSM. In addition to these narrow-width components (NWCs), SNe IIn frequently also exhibit intermediate-width components ((1–4) × 10^3 km s^{-1}, hereafter IWCs) and broad-width components (up to ∼1 × 10^4 km s^{-1}, hereafter BWCs; e.g., Smith et al. 2009). The IWC is likely emitted from a shocked region between the forward and reverse shocks that may consist of accelerated clumps of CSM or of mixed reverse-shocked ejecta and forward-shocked CSM. The BWC could originate from the rapidly expanding ejecta or, at earlier times, may alternatively be the product of electron scattering generating significantly extended wings to the profile.

The X-Shooter spectrum taken on 2010 November 5, 26 days after outburst, shows that SN 2010jl is an SN IIn (Benetti et al. 2010; Yamanaka et al. 2010). In this first spectrum, the Balmer-line profiles are apparently Lorentzian in shape with a narrow peak and broad wings (∼15,000 km s^{-1}). The NWCs in SN 2010jl exhibit P-Cygni profiles (Smith et al. 2011) and are likely sustained at later epochs by X-rays from the shock interaction.

In the optical spectra, the Balmer series and He I lines exhibit IWCs (∼2000 km s^{-1}) from ∼80 days as well as BWCs (Figures 2 and 3). The IWCs increasingly dominate the total line fluxes over time. During the first 200 days, the line profiles (e.g., Hα, Hβ, He I 5876 Å) exhibit a progressive flux bias toward the blue and blueshifted peak fluxes. The blueshifting strengthens through the first 245 days after explosion before receding, much more slowly, back toward zero velocity. The blueshift persists to late epochs (1286 days).

Such red–blue asymmetries could be caused by a number of effects, including high optical depths at early times (Chugai 2001; Smith et al. 2012; Fransson et al. 2014), electron scattering, intrinsic asymmetries in the emissivity distributions, or obscuration of the receding side of the SN by internal dust grains (Lucy et al. 1989).

Several other interacting SNe, such as SN 2005ip, SN 1995N, and SN 2006jd, exhibit similar blueshifted asymmetries in their line profiles (e.g., Stritzinger et al. 2012; Bevan et al. 2019; R. Wesson et al. 2020, in preparation). While an asymmetric geometry could explain the observed line shapes for an individual object, asymmetric geometries are unable to account for both the frequent occurrence of blueshifted emission-line profiles in interacting SNe and the absence of any redshifted equivalents. In addition, the steadily evolving nature of the line asymmetries in SN 2010jl would require a very specific geometry to reproduce the necessary time-dependent emissivity distribution. We therefore disfavor a scenario in which intrinsic geometrical asymmetries are the cause of the asymmetric emission lines in SN 2010jl.

The persistence of asymmetrical lines to very late times (>1000 days) when the photosphere has entirely receded rules out line optical depth effects at late times (Chugai 2018), and, while scattering by electrons in the CSM could cause long-lasting line shifting, it would affect all lines similarly and would not account for the asymmetrical line shapes that are observed. Finally, the simultaneous presence of a significant IR excess combined with the wavelength dependence of the line blueshifting, as discussed by Gall et al. (2014) and Smith et al. (2012), strongly favors a dust formation scenario, with dust grains condensing in a CDS between the shock fronts or in the ejecta itself.

Further, the evolving asymmetries in optical line profiles, first shifting toward the blue by day 112 before returning slowly toward the center over several years, is consistent with an increasing dust mass interior to the forward shock causing greater extinction by dust of emission from the receding side. During the first ∼250–500 days, the strengthening blueshift indicates that the rate of dust formation was high enough to compensate for the drop in the dust optical depth naturally

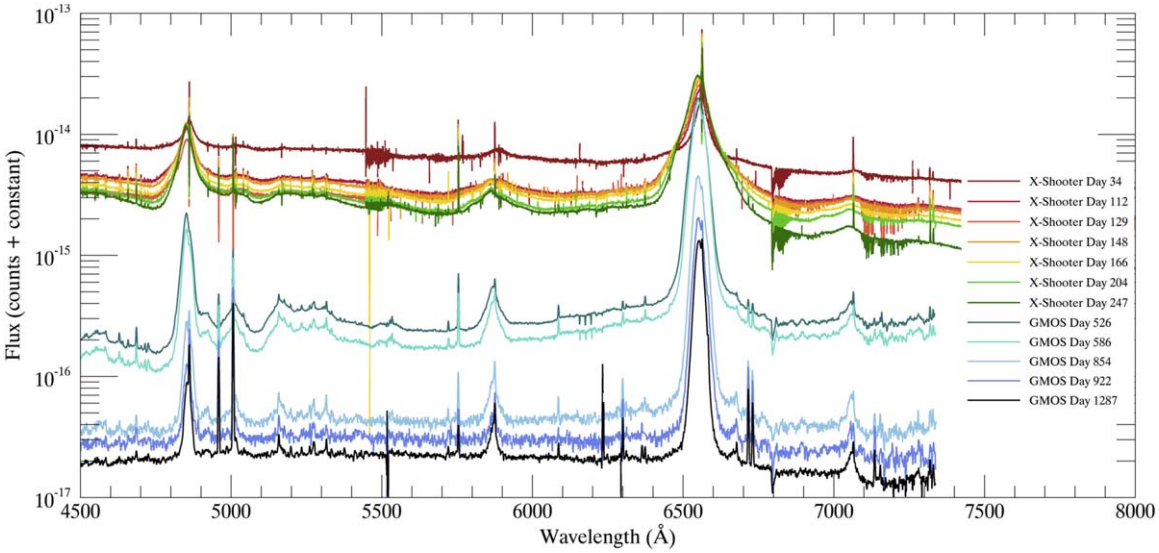

Figure 2. Optical spectra of SN 2010jl from 34 to 1287 days post-outburst. Our late-time Gemini/GMOS spectra are shown in addition to VLT/X-Shooter observations from Gall et al. (2014), which were obtained from the ESO archive. All epochs are relative to our assumed explosion date of 2010 October 10. Note that Gall et al. (2014) adopt epochs relative to SN 2010jl's peak luminosity on 2010 October 18 and thus differ from those given in this paper.
(The data used to create this figure are available.)

caused by the expansion of the system. While the blueshift persists later, its decreasing strength is likely the result of a net decrease in the dust optical depth, due to the expansion of the system dominating over the dust formation rate.

In an expanding medium where lines are broadened by bulk motions, dust grains can only induce line asymmetries where the dust is interior to or colocated with the emitting source. In an SN IIn, red–blue asymmetries in the IWC, such as those seen in SN 2010jl, can only be caused by dust located behind the forward shock. Several dust scenarios could account for red–blue asymmetries in the IWCs of SN 2010jl, e.g., if dust formed rapidly in a CDS between the forward and reverse shocks; if preexisting CSM dust was overrun by the blast wave and a fraction survived; and/or clumps of dust formed in the ejecta which were dense enough to survive the high X-ray luminosity of SN 2010jl (Smith et al. 2012; Chandra et al. 2015). Different populations of dust may account for the observed asymmetries at different times.

Unshocked, preexisting CSM dust cannot account for the observed line asymmetries because it is exterior to the source of the emission and therefore would attenuate the line uniformly across its width. However, the early IR excess could be produced by preexisting dust in the unshocked CSM, warmed by the initial SN flash or by ongoing interactions. It could also be produced by dust in the ejecta or CDS heated either by radiation from the interaction or by radioactive decay. By modeling different dust populations in emission (the SED) and in extinction (the asymmetric line profiles) using two Monte Carlo radiative transfer codes, we have sought to distinguish the different dust populations and to determine their dust masses.

4. Dust Radiative Transfer Models of SN 2010jl

In this section, we describe our approach to modeling the evolving SEDs and blueshifted emission-line profiles of SN 2010jl using MOCASSIN (Ercolano et al. 2003, 2005), which is able to model the dust in emission, and DAMOCLES (Bevan & Barlow 2016; Bevan 2018a, 2018b), which is able to model the effects of dust in extinction on the optical and NIR line profiles, respectively. We have attempted to disentangle preexisting circumstellar dust from dust interior to the forward shock and to infer dust formation rates and dust masses in SN 2010jl.

4.1. Model Geometry

We adopted a geometry that is consistent with observations and able to reproduce both SEDs and line profiles with high-quality fits. A schematic representing our adopted geometry is shown in Figure 4.

Properties of the CSM in SN 2010jl can be inferred from the presence of a strong IR excess at 91 days post-outburst. Andrews et al. (2011) found that the IR excess at this time is likely due to echoing, preexisting circumstellar dust. In order to reproduce the full SED at 91 days, however, the total dust optical depth along the line of sight must be sufficiently low to allow significant optical radiation to escape. Geometries such as a clumpy shell, or inclined lines of sight through a bipolar geometry or torus would allow for this. Andrews et al. (2011) adopted the latter geometry. Our preliminary models with MOCASSIN of a spherically symmetric, homologously expanding ejecta shell ruled out ejecta dust as the source of the IR excess at this epoch, supporting the conclusions of Andrews et al. (2011). We follow their approach and investigate properties of an "outer torus" of echoing circumstellar dust at 91 days post-outburst with the benefit of additional observational data (see Section 4.3.3).

In addition to an outer torus of circumstellar dust, the geometry of the SN system itself can be inferred from the line profiles. Preliminary models and careful visual inspection of the line profiles reveals the simultaneous presence of both a BWC and an IWC in certain lines from ∼80 days. This is particularly clear in the He I 10830 Å line at 247 days and is also present in the He I 20587 Å line; it has been discussed previously by previous authors (Borish et al. 2015; Chugai 2018). We therefore require a

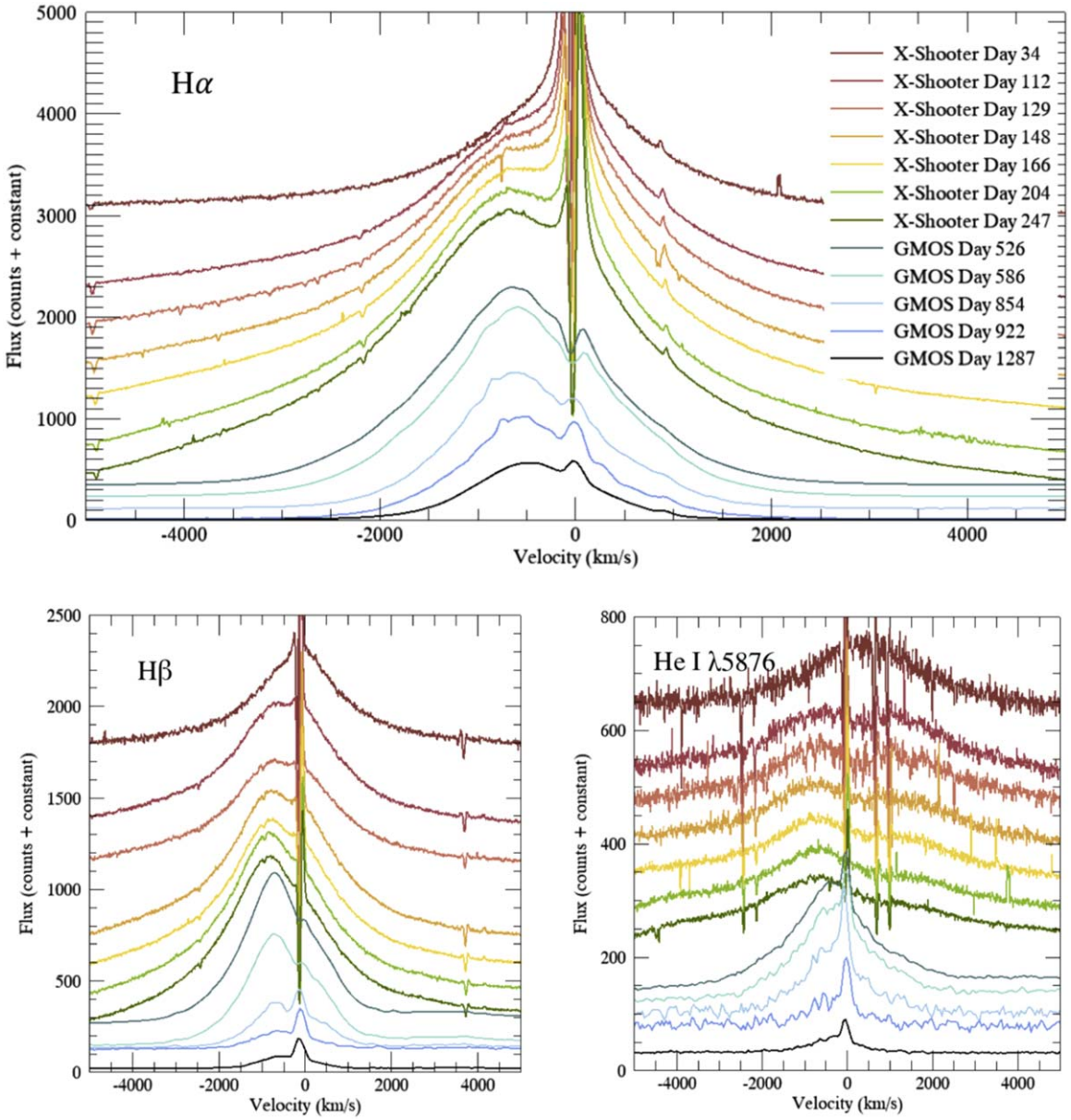

Figure 3. The evolution of the Hα (top), Hβ (left), and He I λ 5876 Å (right) line profiles. We attribute the apparent red peak or shoulder of the He I λ 5876 Å line in the first three epochs to another blended line.

scenario that can produce both components simultaneously. The BWC has been frequently attributed to the effects of electron scattering in SN 2010jl, and this is certainly an important effect at early times (Fransson et al. 2014). At later times, however, the asymmetric, non-Lorentzian shape suggests a alternative origin for the BWC (Gall et al. 2014; Chugai 2018). We therefore attribute the BWC to fast-moving ejecta. To account for the simultaneous presence of both the BWC and the IWC, we presume that the CSM is formed of dense clumps embedded in a more diffuse interclump medium through which the rapidly expanding ejecta can proceed relatively unimpeded. We attribute the IWC to shocked, dense CSM clumps, as has been described by Chugai & Danziger (1994). The CSM clumps may become mixed with reverse-shocked ejecta over time. The early onset of interaction indicates a dense CSM close to the initial explosion. This clumped CSM, which we assume to be distributed in a shell, is therefore distinct from the more distant, echoing outer torus, which our models show must be located at a much greater distance (see Section 4.3.3). A schematic of our adopted geometry is shown in Figure 4, and further details are given below. This model is consistent with the line-profile shapes and the IR echo seen at 91 days. We do not preclude other geometries, and the results that we present here are one possible model that is able to self-consistently reproduce both photometric and spectroscopic observations.

We determined the initial inner radius of the CSM shell based on the appearance of the IWC in the line profiles at ~80 days. We adopted a maximum ejecta expansion velocity of 15,000 km s^{-1} based on the broad wings of the He I 10830 Å line at 247 days assuming minimal contribution from electron scattering. This yielded an initial inner radius for the CSM (prior to outburst) of $R_{\rm in} \sim 1 \times 10^{16}$ cm. The impact of the forward shock with dense CSM clumps propagates a reverse shock back into the ejecta, which we adopted as the inner radius in our models. We evolved the inner radius with time based on the slowest velocities of the postshock region

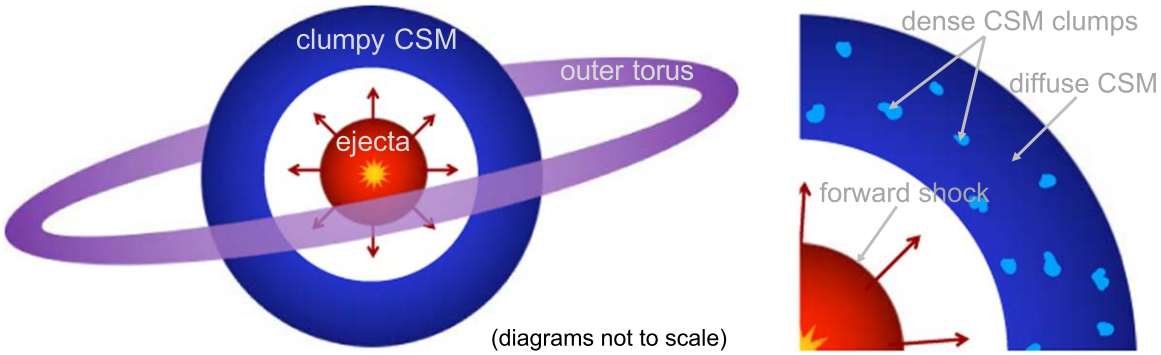

Figure 4. A diagram of a clumpy, inner shell of CSM surrounding the expanding ejecta of SN 2010jl. Upon reaching the CSM, some of the ejecta impact the clumps while some are able to travel freely through the less dense interclump medium. The dusty outer torus is responsible for the IR echo at early times. Only preexisting dust in the outer torus survives the SN flash. Dust forms behind the forward shock in the CSM/ejecta at later times. Similar models have been proposed for SNe IIn such as SN 1988Z and SN 2005ip (Chugai & Danziger 1994; Smith et al. 2009).

(400 km s^{-1} inferred from preliminary line-profile models with DAMOCLES). We presume that the forward shock is able to pass through the more diffuse interclump medium without significant deceleration. We therefore adopted an outer radius of the CSM, $R_{\rm out}$, based on a forward-shock velocity of 15,000 km s^{-1}, calculated independently for each epoch.

CSM clumps were stochastically distributed according to a density distribution $\propto r^{-2}$. Since the majority of material is concentrated toward the inner CSM radius, changes to the outer radius, such as to reduce it based on a decelerating or slower expansion velocity, do not significantly alter our results. Our CSM radius assumptions are supported by our MOCASSIN models, however, which could not reproduce the SED without an extended postshocked region stretching to large radii (see Section 4.3). Initially, a clump volume-filling factor (f) of 0.1 was adopted with clumps of radius $R_{\rm out}/30$. This assumption was investigated and is discussed further in Section 4.2.

The geometry can be summarized as an interior shell of unshocked ejecta impacting a shell of clumpy, shocked material between the forward and reverse shocks, and surrounded by a clumpy shell of unshocked CSM. The entire system is surrounded by an outer torus of dusty CSM. Throughout this paper, we refer to the inner CSM as "CSM" and the outer torus of CSM as the "outer torus."

The concept of the CDS becomes somewhat more complex in this scenario, with an idealized shell of rapidly cooling material seemingly less likely due to the inhomogeneous nature of the CSM. Instead, we presume that the reverse shock generated by impacts between the forward shock and the dense clumps yields numerous rapidly cooling regions of dense material in which dust grains could theoretically form. For ease, we will continue to refer to such regions collectively as a "cool, dense shell" or CDS.

4.2. DAMOCLES Models of SN 2010jl

4.2.1. Radiative Transfer Models of the Blueshifted Hα, Hβ, and He I 5876 Å Lines of SN 2010jl

In order to derive dust masses from observed late-time emission-line profiles in CCSNe, Bevan & Barlow (2016) developed a Monte Carlo radiative transfer code, DAMOCLES, which models the scattering and absorption of line photons by dust in SNe. DAMOCLES allows for arbitrary dust density, emissivity, and velocity distributions to be specified, and any number of dust species and grain size distributions to be investigated.

A range of models treating multiple lines in the spectrum (Hα, Hβ, and He I 5876 Å) simultaneously were developed for three epochs: 526, 915, and 1286 days. These epochs were selected for their coverage of the period of interest and their quality. The lines modeled represented the strongest lines in the spectra and were not significantly contaminated by other nearby lines. By fitting these observed line profiles at a range of epochs, we were able to estimate the mass of dust present in the CDS in SN 2010jl and its evolution over time.

Line photons were emitted from a shell with outer radius $R_{\rm out}$ and inner radius $R_{\rm in}$ representing the positions of the forward and reverse shocks, respectively, as discussed in Section 4.1. An emissivity law $\propto r^{-4}$ was applied, appropriate for recombination in a medium with an inverse-square gas density law, as might be expected for a CSM produced by mass loss at a constant rate. As long as material was predominantly concentrated in the inner regions of the shell, variations in the density distribution of the emitting material did not significantly affect the results.

Due to the complex nature of the dense clumps accelerated by the forward shock, with reverse-shocked ejecta mixing with these CSM clumps due to instabilities caused by the impact, and fast-moving ejecta moving through more diffuse regions between clumps, the typical $v \propto r$ velocity distribution is likely not appropriate in this postshock region. We therefore parameterized the velocity distribution as a power-law velocity $p(v) \propto v^{\alpha}$ independent of radius, with the velocity of an emitting particle sampled from this distribution for every propagated packet. We required that each emitting species followed the same velocity law, but allowed different velocity distributions for hydrogen and helium. The same minimum and maximum velocities were imposed for all emitting species.

The steepness of the velocity law and the minimum and maximum velocities were varied for all three lines simultaneously until good fits to the blue side of the IWC were acquired. Dust was then introduced to the models. We used amorphous carbon grains with optical constants given by the BE sample from Zubko et al. (1996). The lack of observable emission features around 10 μm suggests that the fraction of silicate dust in SN 2010jl is limited and so we considered only amorphous carbon grains for these models (Sarangi et al. 2018). We discuss this assumption further in Section 5.

In order to simultaneously fit Hα, Hβ, and He I 5876 Å, the grain radius of the dust was varied to account for the wavelength dependence of the dust optical depth to which each line was exposed. We found that the dust optical depth to which the Hα and Hβ lines were exposed was very similar, placing strong constraints on the grain radius. A single grain radius was used for these models and, under this assumption, a flat wavelength dependence could only be achieved using grains of at least $a \geqslant 0.1$ μm. Smaller grains have a steeper wavelength dependence that could not simultaneously fit the lines. For smooth models, larger grains would also be inappropriate as they would be too scattering and produce a significant red scattering wing inconsistent with the line profiles. However, clumping suppresses this effect and thus larger grains may be possible in our line-profile models. Further constraints on the grain radius can be derived from the MOCASSIN models, which restrict the grain radius to $a \leqslant 0.3$ μm in all cases. By optimizing both the line-profile fits and the SED fits using a single grain size, we infer grain radii of 0.1 μm at 526 days and 0.2 μm at 915 and 1286 days. It should be noted that distributions of grain radii might alter this inference.

Our conclusions are not necessarily in conflict with suggestions by other authors that there is evidence of a strong wavelength dependence in line extinction because their analyses are based on a wider wavelength range than we have modeled here and they also inferred only small variations in extinction over the wavelength range we consider here (Smith et al. 2012; Moriya et al. 2013; Gall et al. 2014).

The resulting profile fits reproduced the dominant IWC component well, but could not fit the wings of the profile. We therefore considered a modified velocity law, introducing an additional broad component representing the BWC produced by the fast-moving ejecta. Using a similar prescription to the IWC models, we added an additional radius-independent, power-law velocity component at higher velocities such that the velocity distribution was

$$p(v) \propto \begin{cases} v^{\alpha}, & v_{\rm min,IWC} < v < v_{\rm max,IWC} \\ v^{\beta}, & v_{\rm max,IWC} < v < 15,000 \text{ km s}^{-1}, \end{cases} \quad (1)$$

where we impose that the minimum velocity of the broad component is equal to $v_{\rm max,IWC}$ for continuity. We did not change the dust distribution from previous models fixing $f = 0.1$, which we also used for our clumpy MOCASSIN models. The broad-line emission, from the ejecta expanding between the clumps in the CSM, was emitted from between the same inner and outer radii as the IWC. The dust distribution was left unchanged. The introduction of this additional velocity component required only minor changes to the previously best-fitting parameters inferred from just a single IWC. All lines can be simultaneously fitted using the same dust distribution.

Best fits in all cases were obtained through chi-square minimization to the continuum-subtracted emission-line profiles. We estimate the uncertainties in the dust masses to be ~30%. The uncertainties are based on a 10% variation in χ^2 when varying only the dust mass and keeping all other parameters fixed. The He I 5876 Å line was noisy at earlier epochs and so was only considered for verification purposes except at the final epoch at 1286 days.

The final fits to the emission-line profiles are shown in Figure 5, and the parameters and dust masses are listed in Table 4. These models trace dust located in the CDS in the postshock region. The presence of dust in this region of an interacting SN can theoretically be explained in two ways: either new dust grains have formed from heavy elements in the shocked CSM or shocked ejecta or preexisting CSM dust survived the passage of the blast wave. Our models of the light echo at 91 days (see Section 4.3.3) preclude the presence of preexisting dust at radii close to the location of the forward shock (~(0.7–2) $\times$ 10^{17}cm), and we therefore deduce that the dust in the CDS of SN 2010jl is newly formed dust that has condensed in rapidly cooling regions inside dense clumps.

4.2.2. Optically Thick Dust Clumps

One possible limitation of using line profiles to infer dust masses is the possibility that the dust clumps might have high optical depths, obscuring the presence of large masses of dust in their interior (Dwek & Arendt 2015; Dwek et al. 2019). These clumps could be transparent in the IR, and thus visible in emission but not in extinction. Further, highly optically thick dust washes out any wavelength-dependent absorption and makes it difficult to determine properties of the dust grains. We investigated the possibility of optically thick clumps in our models.

Our initial models adopted a volume-filling factor (f) of 0.1 with clumps of radius $R_{\rm out}/30$. We varied the filling factor over a range of values <0.3. Filling factors with $f < 0.03$ only cover a small area of SNe and so do not obscure enough optical emission to reproduce the asymmetries seen in the line profiles. For $f > 0.03$, the line profiles can be reproduced in all cases and, crucially, are still sensitive to the mass of dust in the clumps. Large masses of dust cannot be hidden in clumps when the filling factor is >0.03 and so the dust mass can still be constrained. The dust mass that is required to fit the line profiles does vary slightly as the filling factor is varied between $0.03 < f < 0.3$ by around ~30%. We found only one, very specific case where large masses of dust could be concealed inside optically thick clumps. This was when the filling factor was exactly $f = 0.03$. This specific filling factor results in a dust distribution that covers enough of the SN to attenuate sufficient optical radiation to reproduce the profiles, but also results in clumps that are sufficiently optically thick that they can conceal large (theoretically infinite) amounts of dust. In this case, neither the grain radius nor dust mass can be constrained. However, MOCASSIN models of the SED using a volume-filling factor of $f = 0.03$ are not consistent with large dust masses and are still able to constrain the dust mass, removing this degeneracy (Figure 6). Our final results for the two-component clumped line-profile models with $f = 0.1$ are given in Table 4 and fits can be seen in Figure 5.

4.3. MOCASSIN Models for the SEDs of SN 2010jl

We used the 3D Monte Carlo radiative transfer code MOCASSIN (Ercolano et al. 2003, 2005) to investigate the properties and mass of dust in SN 2010jl. MOCASSIN self-consistently calculates dust temperatures and emission based on any input spectrum, emissivity distribution, and dust grid (Ercolano et al. 2003). For our models of SN 2010jl, the grid was populated with dust with a specified grain size, number density, and composition. The model parameters were then varied to achieve an output SED that matched the observed photometry. The R band was excluded from the fits because it is contaminated by the strong Hα emission. It is noteworthy

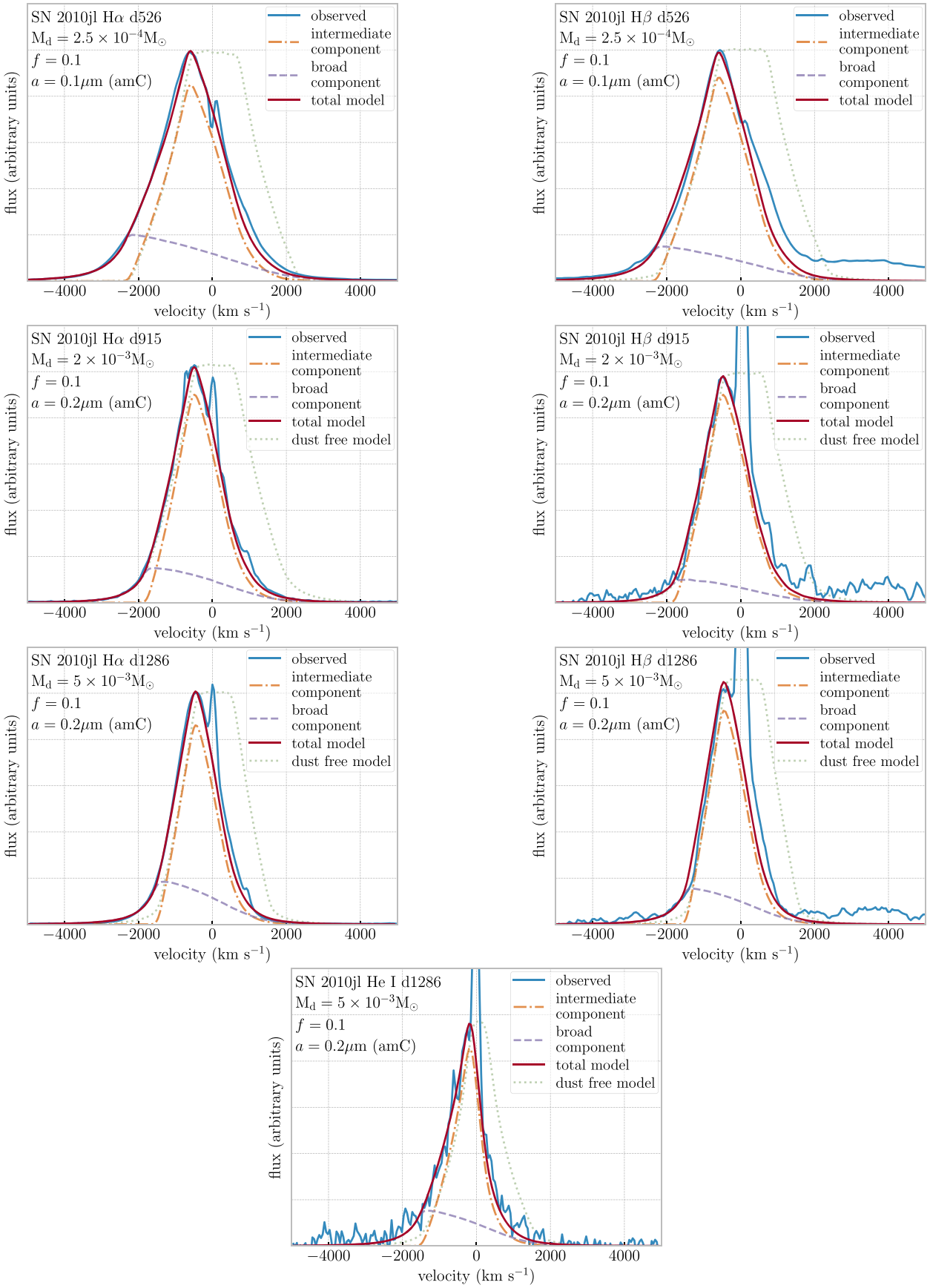

Figure 5. DAMOCLES models of the IWC and BWC of SN 2010jl's strongest optical emission lines, presented in velocity space, for three epochs: 526, 915, and 1286 days. $M_{\rm dust}$ is the total mass of dust, a is the single-size grain radius for amorphous carbon (amC) grains, and f is the clump volume-filling factor set at $f = 0.1$. The narrow emission lines in the observed line profiles (blue solid lines) indicate zero velocity. DAMOCLES models for the IWCs (orange dashed–dotted lines) and the BWCs (purple dashed lines) are combined to produce the final models (solid red lines). Scaled, intrinsic dust-free models are also shown (green dotted lines).

Table 4
Best-fitting Parameters for the Two-velocity Component Clumpy DAMOCLES Models

Line	Epoch (days)	$v_{\rm max,IWC}$ (km s^{-1})	$v_{\rm min,IWC}$ (km s^{-1})	α	β	a (μm)	$M_{\rm dust}$ (10^{-3} $M_\odot$)	$R_{\rm in}$ (10^{16} cm)	$R_{\rm out}$ (10^{16} cm)
Hβ	526	2300	650	0.1	−4.5	0.1	0.25	1.19	6.82
Hα	526	2300	650	0.1	−4.5	0.1	0.25	1.19	6.82
Hβ	915	1800	550	0.3	−4.0	0.2	2	1.33	11.9
Hα	915	1800	550	0.3	−4.0	0.2	2	1.33	11.9
Hβ	1286	1500	500	0.6	−4.0	0.2	5	1.46	16.7
Hα	1286	1500	500	0.6	−4.0	0.2	5	1.46	16.7
He I λ 5876	1286	1500	200	0.1	−4.0	0.2	5	1.46	16.7

Note. The parameters are defined as follows: $v_{\rm max,IWC}$ and $v_{\rm min,IWC}$ are the maximum and minimum velocities for the IWC, respectively. α is the radius-independent gradient of the velocity distribution for the IWC; see Equation (1). β is the gradient of velocity distribution for the BWC, which has a maximum velocity of 15,000 km s^{-1} and a minimum velocity equal to the IWC maximum velocity ($v_{\rm max,IWC}$) for continuity (see Equation (1)). $M_{\rm dust}$ is the total mass of the dust, and $R_{\rm out}$ and $R_{\rm in}$ are the outer and inner radii of the postshock region, respectively.

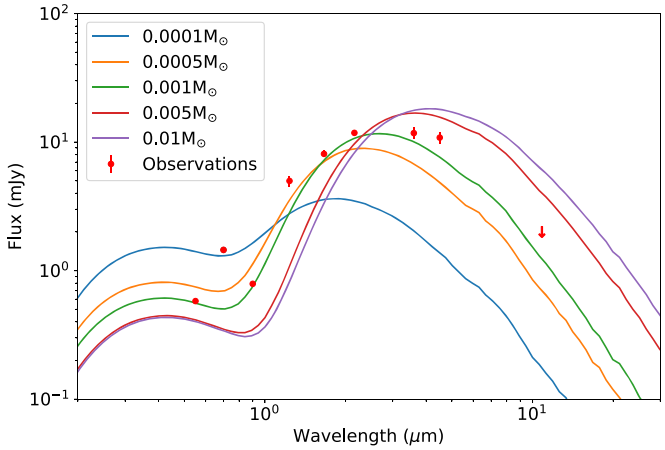

Figure 6. MOCASSIN SEDs for a clump-filling factor of $f = 0.03$ and observations at 464 days. Emission-line profiles are not sensitive to the dust mass for this particular filling factor, but the SED remains so.

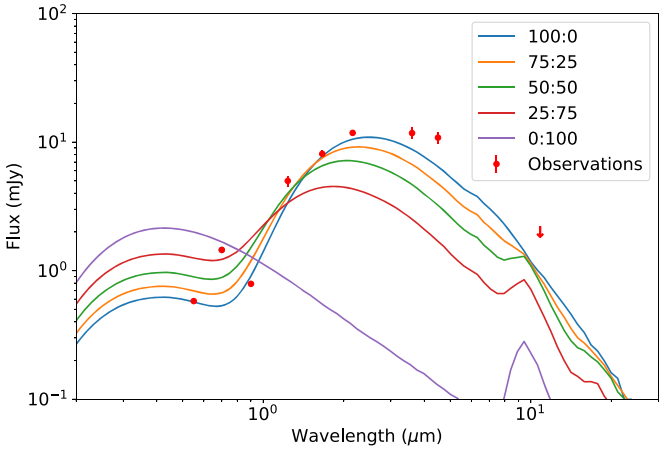

Figure 7. Predicted SEDs for 7×10^{-4} $M_\odot$ of dust with composition indicated in the key as the amorphous carbon:silicates ratio. Observations are at 464 days. Nonzero silicate fractions result in too much optical emission escaping and not enough infrared emission to fit the observed excess.

that the models can only put constraints on warm dust as there are no observations longward of 4.5 μm. Colder dust may be present and emitting at longer wavelengths.

4.3.1. Amorphous Carbon Dust Grains

As per our DAMOCLES models, we adopt a pure amorphous carbon dust composition using optical constants from the BE sample of Zubko et al. (1996). There have been nondetections of SN 2010jl at 10.7 μm with VLT/VISIR on day 519 (see Section 2) and at 11.1 μm with SOFIA/FORCAST on day 1304 (Williams & Fox 2015). These nondetections provided upper limits of 2 mJy and 4.2 mJy, respectively, on the brightness of any 9.7 μm silicate feature present in SN 2010jl. Models of optically thin silicate dust emission by Williams & Fox (2015) predicted a flux at 11 μm significantly exceeding these upper limits. Our own MOCASSIN models of silicate dust in dense clumps confirm that silicate dust gives very poor fits to the SED. Figure 7 shows the predicted emission from 7×10^{-4} $M_\odot$ of dust, composed of pure silicates, pure amorphous carbon, and three mixed compositions. These SEDs show that an amorphous carbon fraction close to 1 is required to provide clumps that are opaque at optical wavelengths and emit efficiently enough to reproduce the observed infrared excess. Even significantly larger masses of silicate dust (>0.01 $M_\odot$) are unable to sufficiently attenuate the optical. It is possible that silicates make up a nonzero fraction of the grain composition, but we infer that carbon grains dominate the emission and therefore use 100% amorphous carbon grains in our models. We investigated a range of single grain sizes $\geqslant$0.1 μm based on our DAMOCLES models. We adopted the grain size that yielded optimal fits for both the SED and line profiles at each epoch.

4.3.2. How is the Dust Heated?

There are several mechanisms that could be heating the dust, depending on its location. Radioactive decay would only affect the ejecta dust, and we do not account for this explicitly in our models. Even if our models did account for it, the very high IR luminosity means that ejecta dust heated by radioactive decay cannot be significantly contributing. To emphasize the size of the IR excess, a comparison of the SEDs for SN 1987A on day 615 and SN 2010jl on day 621 are presented in Figure 8. Radioactive heating depends on the nickel mass, and for SN 1987A, that is about 0.1 $M_\odot$ (Seitenzahl et al. 2014). In Figure 8, the SEDs are at the same epoch and scaled to the same distance, and there is about four orders of magnitude more dust luminosity from SN 2010jl. Ofek et al. (2019) preformed a similar exercise by showing that 1 $M_\odot$ of ^{56}Ni was not enough to reproduce the light curve.

A far more important contributor to heating the dust is the interaction between the ejecta and the CSM. The high-energy

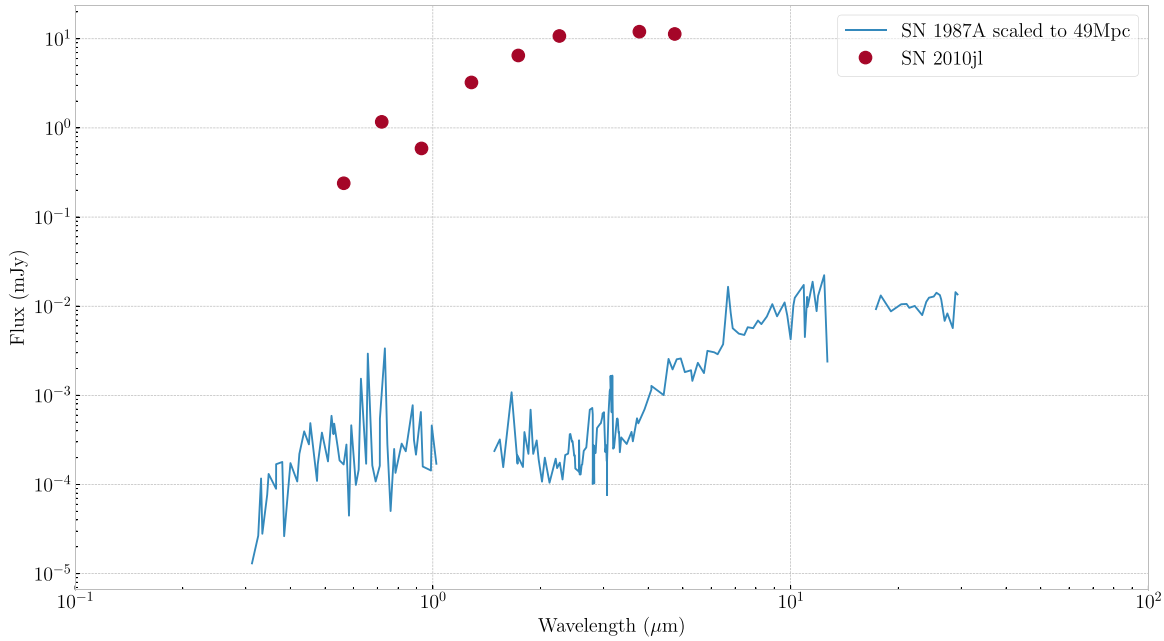

Figure 8. The SEDs of SN 1987A (Wooden et al. 1993; Wesson et al. 2015) and SN 2010jl on days 615 and 621, respectively. The flux densities from SN 1987A are scaled for the distance of SN 2010jl. While SN 2010jl was an X-ray and optically luminous SN, it also has a very large IR excess. Its dust luminosity is too large to only be dust warmed by radioactive decay.

photons, emitted by the interaction, will heat the surrounding dust, new and preexisting. Our models include a simplified version of this interaction region in MOCASSIN by using a diffuse light source that is colocated with the dust, simulating the dust being heated by the gas, which is itself heated by the energetic interaction. The variables for this source of photons are temperature, luminosity, radius, and number of photons. Adopting the same radii as the DAMOCLES models, we include an internal, clumpy shell representing the postshocked region as well as an outer torus of flash-heated dust.

A third heating source is the SN flash, seen as a thermal echo in the outer torus. Andrews et al. (2011) took the IR excess at 91 days together with the very small line-of-sight extinction to imply an asymmetric CSM, with no dust along the line of sight. They adopted an inclined torus of CSM. The models described in that paper predict the evolution of the IR flux as the flash propagates through the torus.

4.3.3. The Evolution of the Thermal Echo

The first epoch we modeled with MOCASSIN was 91 days. Building on the work of Andrews et al. (2011), we were able to fit the IR excess at this epoch with an IR echo from the SN flash illuminating an outer torus of CSM (see Figure 4). The 4.5 μm flux is higher than the 3.6 μm flux at this epoch, requiring the dust to be relatively cool and thus ruling out ejecta dust. We used the following flash source parameters: a central point source with a blackbody continuum of temperature of 15,000 K and a luminosity of $8 \times 10^9\ L_{\odot}$. For the echo model, we began with the same parameters as Andrews et al. (2011), who used the combination of negligible line-of-sight optical depth and infrared excess to propose that the CSM was in a torus, with a radius of 1.2 lt-yr and a tube radius of 0.5 lt-yr, inclined at 60° to the plane of the sky. The additional data available since then provide further constraints, which we used to refine our model. In particular, the nondetection of SN 2010jl at 10.7 μm on day 519 means that the CSM must have a smaller outer radius than initially proposed by Andrews et al. (2011). We find that a radius of 1.0 lt-yr and a tube radius of 0.3 lt-yr fits the day 91 SED while not violating the constraints at day 519. This revised geometry has its inner edge at the same distance as the earlier model. The inner edge of the torus is significantly beyond the location of the forward shock at all epoch considered in this paper. Any preexisting dust located at radii inside the torus would be too hot to be consistent with the SED at 91 days. We therefore infer that there is no preexisting CSM dust interior to this torus. We find that a total dust mass of $0.015\ M_{\odot}$ is required to fit the SED. We assumed that the outer torus dust mass estimate at 91 days is the total mass of dust in the torus and that it does not change from this onwards.

At later epochs, the total SED therefore consists of the echo from the outer torus plus emission from newly formed dust in the CDS and/or ejecta located interior to the forward shock. The echo models were calculated based on a flash of 100 day duration and integrating the emission from grid cells that lie between the two ellipsoids that corresponded to the beginning and end of the flash. The echo accounts for the entirety of the IR excess at 91 days, makes a small contribution at 450–550 days, and is no longer present by 996 days (see Figure 9).

4.3.4. Radiative Transfer Models of the SEDs of SN 2010jl

We ran a series of models for the later epochs (at 464, 525, 996, and 1367 days) in which we put dust inside the forward-shock radius ($R_{\rm out}$) with an r^{-2} density distribution and diffuse photon source representing heating from the gas which has itself been heated by high-energy radiation from the interaction of the ejecta with the CSM. All models maintained fixed radii, calculated as per Section 4.1 and listed in Table 5). A 100% pure amorphous carbon dust composition was used with grains of $a \geqslant 0.1$ μm radius, based on the DAMOCLES results. At each epoch, the dust mass, filling factor, source temperature, grain radius, and source luminosity were varied to obtain best fits to

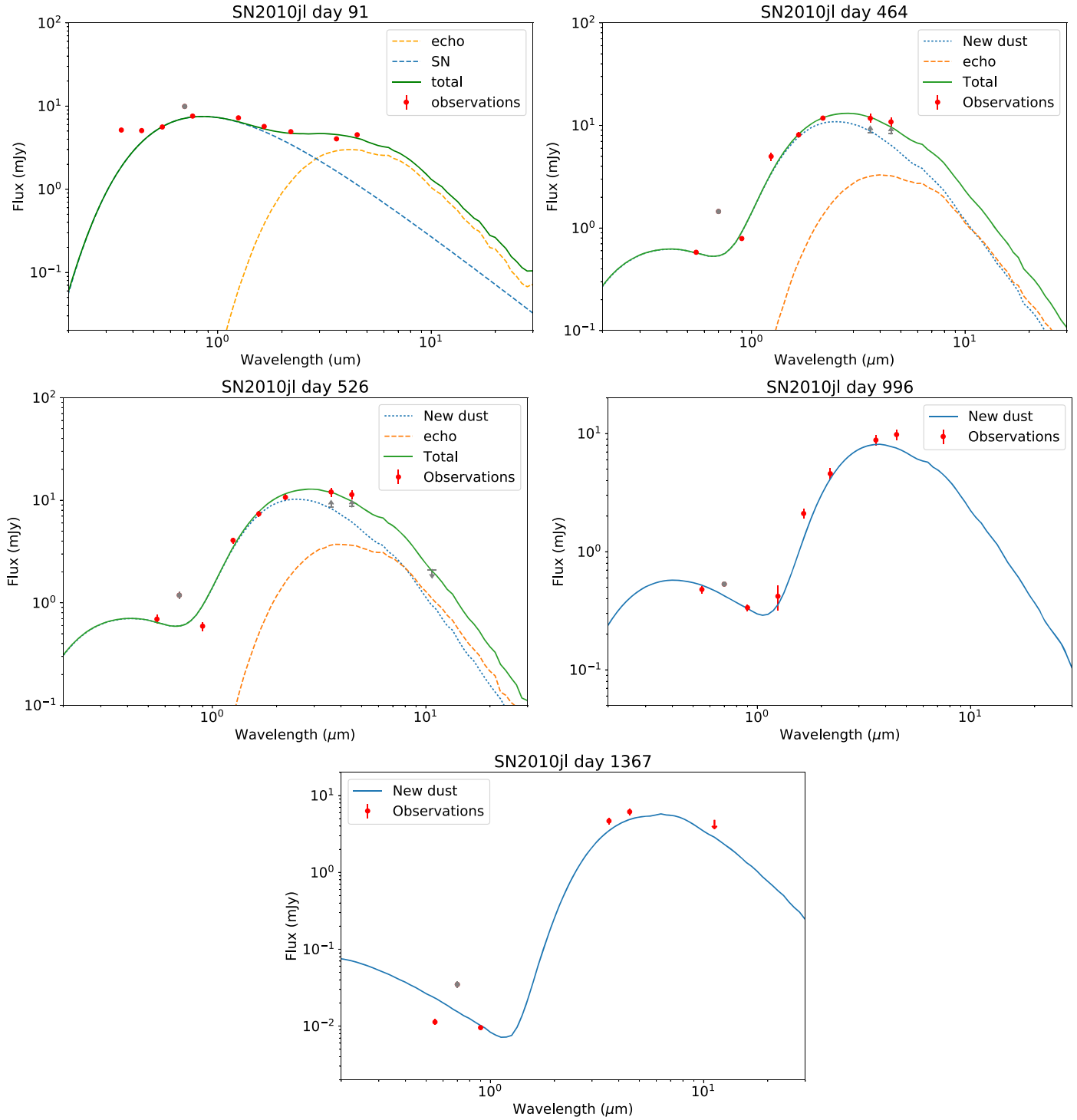

Figure 9. The results of the MOCASSIN models, with data points in red. The optical and *JHK*s points are a combination of our data and those of Fransson et al. (2014), where we used data from the days closest to our mid-IR observations. We do not attempt a fit to the *R*-band data as they contain the strong Hα emission line. The saturated Spitzer fluxes at 464 and 526 days are shown as a lower limit in gray. The VISIR 10.7 μm upper limit at 526 days is also shown in gray. Top left: the fit to day 91 showing that the IR can be accounted for by just the flash echo (orange). Top right: the fit to day 464 shows that the echo is still relevant (orange), but the IR emission is dominated by the dust in the ejecta/CDS (blue). The sum of these components is shown in green. Middle left: day 526 is very similar to day 464. Middle right: by day 996, the SN flash is no longer illuminating the CSM that was echoing at day 91, and the IR emission is coming entirely from new dust (blue). Bottom: similar to day 996, but with a constraining upper limit at 11.1 μm.

the observations (excluding the *R* band). A summary of the best-fitting parameters is given in Table 5, and the fits are presented in Figure 9.

At day 464, a clumped distribution allowed for better fits than a smooth distribution of dust, which did not allow enough optical emission to escape. We adopted a filling factor of $f = 0.1$ for consistency with the line-profile models. We found that a source luminosity of $\sim 2 \times 10^9\,L_\odot$ was optimal. The total mass of newly formed dust for day 464 was $7 \times 10^{-4}\,M_\odot$. At 519 days, the 10.7 μm upper limit from VLT/VISIR does not

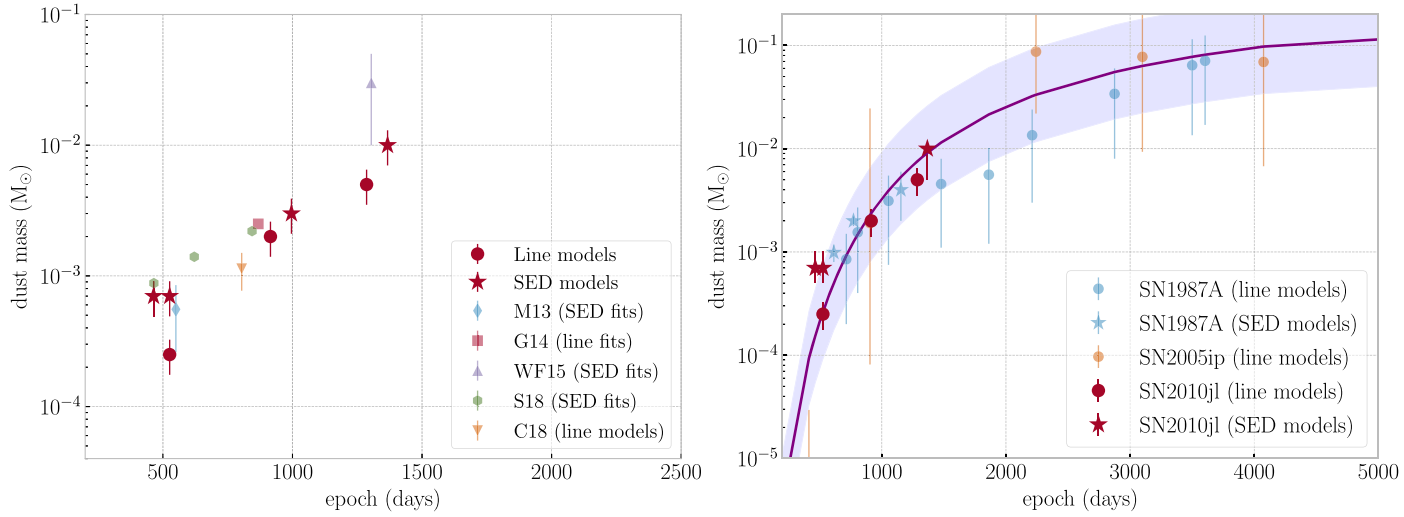

Figure 10. The dust mass ($M_\odot$) evolution of SN 2010jl. The results of our MOCASSIN and DAMOCLES modeling are shown above in red stars and circles, respectively. On the left are additionally plotted dust mass estimates for SN 2010jl from Maeda et al. (2013), Gall et al. (2014), Williams & Fox (2015), Sarangi et al. (2018), and Chugai (2018), labeled as M13, G14, WF15, S18, and C18, respectively. On the right, dust mass estimates for SN 2005ip from line-profile models (Bevan et al. 2019) and for SN 1987A from line-profile models (Bevan & Barlow 2016) and SED models (Wesson et al. 2015) are also plotted along with the curve of best fit from Bevan et al. (2019).

Table 5
Best-fitting Parameters for the MOCASSIN Models

Age (days)	T_{source} (1000 K)	L_{source} (10^9 $L_\odot$)	f	a (μm)	New dust mass ($M_\odot$)	Echoing dust mass ($M_\odot$)	R_{in} (10^{16} cm)	R_{out} (10^{16} cm)
91	17.5	7.97	1.0	0.02	...	0.015	66.2†	123†
464	12	1.8	0.1	0.1	7×10^{-4}	0.015	1.17	6.0
526	12	1.8	0.1	0.1	7×10^{-4}	0.015	1.19	6.8
996	12	1.2	0.1	0.2	3×10^{-3}	0.015	1.36	12.9
1367	30	0.4	0.1	0.2	1×10^{-2}	0.015	1.48	17.7

Note. The parameters are defined as follows: T_{source} and L_{source} are the temperature and luminosity of the illuminating blackbody, respectively, f is the clump volume-filling factor, a is the single grain radius, and R_{out} and R_{in} are the outer and inner radii of the postshock region, respectively. Note that the parameters given for 91 days are solely for echoing dust in the outer torus, the inner and outer edges of which are specified by R_{in} and R_{out} and marked with a †.

allow for very much dust emitting at that wavelength, thus additionally constraining the outer radius of the echoing torus. This upper limit also precludes the presence of a significant fraction of silicate grains.

On day 996, newly formed dust behind the forward shock is much more important than dust in the echoing torus. While a reasonable fit to the SED can be obtained with grains of radius $a = 0.1$ μm, an improved fit can be obtained with grains of radius $a = 0.2$ μm. The mass of newly formed dust at this epoch had increased from 7×10^{-4} $M_\odot$ at day 464 to 3×10^{-3} $M_\odot$ at 996 days.

By day 1367, the dust mass required to fit the SED was 1.0×10^{-2} $M_\odot$ using grains of radius $a = 0.2$ μm. A smooth distribution produced a slightly improved fit, but the clumped distribution, which is also a good fit, is consistent with the DAMOCLES results.

5. Discussion

Our radiative transfer models fitting both dust emission and extinction in SN 2010jl have allowed us to determine dust masses at a range of epochs. By fitting the dust emission in the near- and mid-IR, we were able to determine the dust mass emitting in the CSM, CDS, and ejecta in SN 2010jl. We have been able to construct a scenario for SN 2010jl whereby the SN ejecta is interacting with a clumpy CSM that is consistent with both photometric and spectroscopic observations over several years. We have obtained extremely good fits to the line profiles and SEDs at a range of epochs. We group our models into four epochs for the sake of comparing our SED and line profiles results for SN 2010jl on days 91, 464 and 526, 996 and 915, and 1286 and 1367. Figure 10 summarizes our results and compares them to those from other studies of SN 2010jl and with other SN dust mass estimates.

Our dust mass estimates using MOCASSIN for the first epoch (day 91) reveal that the IR emission can be entirely accounted for by flash-heated preexisting dust in an outer torus of circumstellar material. This is in agreement with the findings of Andrews et al. (2011), with a slightly lower outer radius for the torus. Assuming that the total gas mass of the CSM is 10 $M_\odot$ (Ofek et al. 2014; Sarangi et al. 2018) and a gas-to-dust ratio of 200, there should be $\sim$0.05 $M_\odot$ of preexisting echoing dust (Draine et al. 2007). Our MOCASSIN estimate of the echoing dust mass at this epoch is 0.015 $M_\odot$, which is entirely preexisting dust, consistent with the above mass estimate considering the large uncertainties in the CSM mass, the gas-to-dust ratio, and the location of the circumstellar material. Some preexisting CSM dust may have been vaporized by the initial SN flash, but the early IR emission indicates that a

significant mass of CSM dust survived, at least at the radius of the outer torus (∼0.7 lt-yr). This preexisting dust associated with pre-SN mass-loss phases would have been more likely to survive the flash if it was distributed in an asymmetric geometry which provided a high dust optical depth along some lines of sight, e.g., a torus or bipolar geometry, as we have inferred here and in Andrews et al. (2011).

The data for the second epoch were obtained at 464 days for Spitzer and at 526 days for the optical spectra and photometry. As shown in Figure 1, there is a gap in the data from 260 to 373 days. After this gap, the SN had become much brighter in the near- and mid-IR, and the red–blue emission-line asymmetries had strengthened, indicating the presence of dust in the ejecta and/or CDS (see Figure 3). Also during this period, the visible light curve begins a steeper decline. This drop in the optical could be attributed to a number of causes (see Ofek et al. 2019), but its coincidental timing with the sharp rise in the IR and increasing line asymmetries may indicate a link with the onset of dust formation in the CDS or ejecta. The first observations after the gap were on day 374 (*JHK*s) and day 464 (Spitzer). There is a much larger IR excess at *HK*s and at 3.6 and 4.5 μm than was observed before the gap. Our models reveal that a small contribution from preexisting, echoing dust in the CSM (see Figure 9) still persists at day 464. The MOCASSIN model on day 464 also requires new dust with a mass of $8 \times 10^{-4}\,M_{\odot}$. The first dust mass estimate using DAMOCLES is $2.5 \times 10^{-4}\,M_{\odot}$ for day 526. We discuss the small discrepancy between these dust mass estimates in more detail below.

The data for the third epoch were obtained at 996 days for Spitzer and at 915 days for the optical spectra. MOCASSIN models were able to constrain the dust grain radius at this epoch to ∼0.2 μm. Consistent line-profile fits were obtained using DAMOCLES using this grain radius. The SED models yielded a mass of new dust of $3 \times 10^{-3}\,M_{\odot}$, while at a similar epoch (day 915), the DAMOCLES models required a dust mass of $2 \times 10^{-3}\,M_{\odot}$. These masses are in good agreement with each other, suggesting that the SED is likely tracing all new dust at this epoch. Gall et al. (2014) estimated a dust mass of $\sim 10^{-3}\,M_{\odot}$ at 868 days. This estimate depends on emission out to just the *Ks* band and so is not sensitive to cooler dust emitting in the Spitzer bands and so is broadly consistent with our estimates here. Their inference that larger dust grains are required to account for the line profiles is also in agreement with our conclusions that single-size grains of radius ∼0.2 μm are required. While they require a much larger maximum grain size of 4.2 μm, their use of a power-law distribution of grains steepening toward smaller grains makes direct comparison with our single grain size difficult.

In our final epoch (1367 days for our SED models and 1286 days for the optical spectra), the ejecta has now reached $\sim 2 \times 10^{17}$ cm and is significantly mixed with shocked CSM clumps. A slightly improved fit to the photometric observations could be obtained using a smooth distribution instead of simply expanding the model used at previous epochs with a clump volume-filling factor of 0.1. However, the DAMOCLES models are inconsistent with a smooth dust distribution at this epoch, requiring clumping to suppress the extended red scattering wings produced by larger grains, which are themselves required to reproduce the observed wavelength dependence of the line asymmetries. The mass of dust inferred from DAMOCLES models reaches $5 \times 10^{-3}\,M_{\odot}$ by day 1286. The total warm dust mass of SN 2010jl based on the MOCASSIN models has also increased, reaching $1 \times 10^{-2}\,M_{\odot}$ on day 1367. A plot of the newly formed dust mass evolution over time, as determined by our SED and line-profile fits, is presented in Figure 10.

5.1. The Location of the Dust in SN 2010jl

Using two independent methods, we have traced the dust in SN 2010jl yielding broadly consistent results. However, a small discrepancy is seen between the methods, with SED-derived dust masses being slightly higher than those derived from line profiles. These differences are within the uncertainties, but we discuss possible physical causes below.

A limitation of modeling the line profiles of interacting SNe is the relative extents of the line-emitting region and the unshocked ejecta. As the projected area of the unshocked ejecta is small compared to the line source, it is possible to hide significantly large masses of dust in the unshocked ejecta that do not significantly affect the line profiles. In the case of SN 2010jl, our models showed that large masses of dust in the unshocked ejecta would have only a very small effect on the shape of the line profiles. We therefore emphasize that the masses of dust inferred from our line-profile models of SN 2010jl must be located in the postshocked region.

Our SED models, adopting the same geometry as our line-profile models, required slightly higher dust masses to reproduce the observed SED. These models were somewhat insensitive to the inner radius of the emitting, dusty shell. Reducing the inner radius to much smaller values of $R_{\rm in}$ than given above did not alter the dust mass required to fit the SED. This new geometry, with smaller inner radii, could be interpreted as a single shell representing both the postshock region and the unshocked ejecta, though clearly a single power-law density distribution representing both regions is likely a significant simplification of the true geometry. Nonetheless, it suggests the possibility that the emitting dust traced by our SED models could be newly formed warm dust in the unshocked ejecta or dust in the postshocked region (or a combination). This may account for the discrepancy with the line-profile models that traced only CDS dust.

We note the theoretical possibility that the presence of cold dust in the unshocked ejecta radiating in the FIR could evade both techniques. While we have confirmed that the line profiles would indeed be insensitive to such cold dust, the intense radiation emitted by the reverse shock would heat (or evaporate) any dust in the unshocked ejecta causing it to appear in the SED. Only in cases of extreme clumping might it be possible for cold dust to avoid being heated. The possibility of ejecta geometries that could plausibly hide significant cold dust masses will be the subject of a future paper (A. Bevan & R. Wesson 2020, in preparation). We conclude that the total mass of newly formed dust within SN 2010jl cannot be significantly higher than our dust mass estimates.

5.2. The Origin of the Dust in SN 2010jl

Throughout this work, we have attributed the presence of dust in the postshocked region of SN 2010jl to newly formed dust that has condensed in rapidly cooling regions from either shocked ejecta or shocked CSM. An alternative explanation for the presence of dust in the postshocked region of SN 2010jl at later times is that preexsiting CSM dust was overrun by the forward shock but survived its passage to enter the postshocked

region. However, for the adopted torus geometry, our models at 90 days preclude the presence of dust at radii $\lesssim$0.7 lt-yr. Preexisting dust at smaller radii is heated to higher temperatures than dust farther from the illuminating flash. The NIR and MIR SEDs can therefore constrain the location of any flash-heated, preexisting dust, and our 90 day model ruled out dust interior to ∼0.7 lt-yr. By ∼1300 days, a forward shock traveling at 15,000 km s^{-1} would have reached a distance of 0.18 lt-yr. The lack of dust at radii $\lesssim$0.7 lt-yr at 90 days is therefore inconsistent with this explanation. We infer that new dust formation interior to the forward shock is required to account for the dust present in SN 2010jl at later times.

5.3. Comparison with Other Dust Mass Estimates

Several previous works have also concluded that new dust is forming in SN 2010jl, with a range of estimated dust masses in various locations. We compare our dust mass estimates for SN 2010jl with those from the literature in the left panel of Figure 10.

Maeda et al. (2013) estimated (7.5–8.5) × 10^{-4} $M_{\odot}$ of new dust was present in SN 2010jl at 550 days post-outburst, which started forming ∼1 yr post-explosion. Their analysis was based on the NIR SED, balancing the mass of dust required to produce the emission in the NIR with the absorption required to reproduce the optical data. As might be expected, this is in agreement with our day 464 MOCASSIN dust mass estimate but, like our own SED-derived dust mass estimate, is somewhat larger than the dust mass inferred from our line-profile modeling at day 526. Maeda et al. (2013) further concluded that the dust was likely located in clumps with a filling factor of ∼0.1, consistent with our model assumptions. Similarly, Smith et al. (2012) inferred that dust may have formed before 500 days based on the presence of an early IR excess and the wavelength-dependent asymmetries exhibited by the optical and NIR emission lines.

Gall et al. (2014) conducted a detailed study of the extent of the red–blue asymmetries in the optical and NIR emission lines, concluding that, for a power-law grain radius distribution, the maximum grain radius must be large (4.2 μm) to account for the observed wavelength dependence. Our line-profile models are restricted to a relatively narrow wavelength range (4861–6563 Å) over which we see little variation in the dust optical depth. Given the uncertainties involved and the narrow wavelength range investigated in this work, we do not conclude that there is any conflict with the conclusions of Gall et al. (2014) or Smith et al. (2012), who highlight strong wavelength dependence in the asymmetries of the optical and NIR line profiles. Gall et al. (2014) proposed a rapid (40–240 days) formation of carbonaceous dust in the CDS. At later times (500–900 days), they concluded that the dominant dust emission component has transitioned to the ejecta. By 868 days, their inferred dust mass was 2.5 × 10^{-3} $M_{\odot}$, in strong agreement with our dust mass estimate of 2 × 10^{-3} $M_{\odot}$ inferred from our line-profile fits and 3 × 10^{-3} $M_{\odot}$ inferred from our SED fits.

Chugai (2018) conducted a similar modeling of the optical and NIR line profiles of SN 2010jl, reaching similar conclusions regarding the origins of the BWC in the rapidly expanding ejecta and the IWC in dense CSM clumps. Though he restricted his analysis to studies of the necessary optical depths and albedos required to reproduce the line profiles, he suggested that, for a grain radius distribution 0.001 μm < a < 0.1 μm with $n(a) \propto a^{-3.5}$, 1.5 × 10^{-3} $M_{\odot}$ of graphite dust in the unshocked ejecta and CDS would be required to fit the line profiles at 804 days post-outburst, again in broad agreement with our conclusions at similar epochs.

Sarangi et al. (2018) suggested that the IR emission observed prior to 380 days must be the product of a light echo because dust would not be able to form during the first year of SN 2010jl's evolution. We did not investigate new dust formation during this period. However, we were not able to fit the SED at 91 days with a pure ejecta dust model and find, in agreement with Sarangi et al. (2018), that a pure echo model is able to entirely account for the observed photometry. While the contribution from the echo is still important at 464 days, the dominant dust emission component has transitioned to the ejecta/CDS by this time. Sarangi et al. (2018) estimated interior dust mass of 8.8 × 10^{-4} $M_{\odot}$, 1.4 × 10^{-3} $M_{\odot}$ and 2.2 × 10^{-3} $M_{\odot}$ at 465 days, 621 days and 844 days, respectively, for an amorphous carbon composition. These estimates closely follow our inferred dust mass estimates.

We compare our dust mass estimates for SN 2010jl to dust mass estimates obtained using detailed radiative transfer models for other CCSNe in Figure 10. We compare SN 2010jl specifically to SN 2005ip, as a much less luminous but still dusty SNe IIn for which the dust evolution has been previously investigated (Bevan et al. 2019). We also compare our results to the dust evolution of SN 1987A as the best-known and most analyzed dust-forming core-collapse SN (e.g., Wesson et al. 2015; Bevan & Barlow 2016). We plot the curve of best fit derived for SN 2005ip by Bevan et al. (2019). There is strong agreement between the dust mass estimates derived for all three of these objects, and similar trends in their dust mass evolution are observed. This is perhaps surprising given differences in their intrinsic types, progenitors, and progenitor masses. We conclude that SN 2010jl is likely to continue forming dust in its ejecta/CDS and that future spectral and photometric observations of SN 2010jl will help to determine its final dust mass.

6. Conclusions

Through the use of two complementary radiative transfer codes, we have been able to determine the masses and evolution of different dust populations in SN 2010jl over the first 1400 days. We find that an IR echo is able to account for the observed IR excess at 91 days but that low line-of-sight optical depths are required. We find that the IR echo makes only a small contribution to the observed IR flux by 464 days and makes no contribution by 996 days. The presence of dust behind the forward shock is required to account for both the blueshifted optical emission-line profiles and the observed IR excess. We have modeled both of these observational signatures of dust in SN 2010jl and have found a dust mass that increases from (2.5–7) × 10^{-4} $M_{\odot}$ at ∼500 days to (0.5–1)×10^{-2} $M_{\odot}$ by ∼1400 days. We have compared our results to the conclusions of other authors and find them to be in generally good agreement. Future observations will be necessary to follow the ongoing formation of dust in SN 2010jl.

We are grateful for the support provided by the Ball Family Distinguished Professor endowment. This work was also supported by Spitzer Space Telescope RSA 1439444 and RSA 1415602, issued by JPL/Caltech, and by European Research Council (ERC) Advanced Grant SNDUST 694520.

We thank the anonymous referee for their detailed review and constructive suggestions and comments.

Facilities: Gemini (GMOS), VLT (X-SHOOTER), NTT (SOFI), Spitzer (IRAC).

Software: IRAF (Tody 1986, 1993); ESOREX (Freudling et al. 2013); MOCASSIN (Ercolano et al. 2003); DAMOCLES (Bevan & Barlow 2016; Bevan 2018b).

ORCID iDs

A. M. Bevan https://orcid.org/0000-0001-7188-6142
J. E. Andrews https://orcid.org/0000-0003-0123-0062
M. J. Barlow https://orcid.org/0000-0002-3875-1171
G. C. Clayton https://orcid.org/0000-0002-0141-7436

References

Andrews, J. E., Clayton, G. C., Wesson, R., et al. 2011, AJ, 142, 45
Benetti, S., Bufano, F., Vinko, J., et al. 2010, CBET, 2536, 1
Bevan, A. 2018a, MNRAS, 480, 4659
Bevan, A. 2018b, DAMOCLES: Monte Carlo Line Radiative Transfer Code, Astrophysics Source Code Library, ascl:1807.023
Bevan, A., & Barlow, M. J. 2016, MNRAS, 456, 1269
Bevan, A., Barlow, M. J., & Milisavljevic, D. 2017, MNRAS, 465, 4044
Bevan, A., Wesson, R., Barlow, M. J., et al. 2019, MNRAS, 485, 5192
Borish, H. J., Huang, C., Chevalier, R. A., et al. 2015, ApJ, 801, 7
Cardelli, J. A., Clayton, G. C., & Mathis, J. S. 1989, ApJ, 345, 245
Chandra, P., Chevalier, R. A., Chugai, N., Fransson, C., & Soderberg, A. M. 2015, ApJ, 810, 32
Chandra, P., Chevalier, R. A., Irwin, C. M., et al. 2012, ApJL, 750, L2
Chevalier, R. A., & Fransson, C. 1994, ApJ, 420, 268
Chugai, N. N. 2001, MNRAS, 326, 1448
Chugai, N. N. 2018, MNRAS, 481, 3643
Chugai, N. N., & Danziger, I. J. 1994, MNRAS, 268, 173
Draine, B. T., Dale, D. A., Bendo, G., et al. 2007, ApJ, 663, 866
Dwek, E., & Arendt, R. G. 2015, ApJ, 810, 75
Dwek, E., Sarangi, A., & Arendt, R. G. 2019, ApJL, 871, L33
Ercolano, B., Barlow, M. J., & Storey, P. J. 2005, MNRAS, 362, 1038
Ercolano, B., Barlow, M. J., Storey, P. J., & Liu, X.-W. 2003, MNRAS, 340, 1136
Fox, O. D., Filippenko, A. V., Skrutskie, M. F., et al. 2013, AJ, 146, 2
Fransson, C., Ergon, M., Challis, P. J., et al. 2014, ApJ, 797, 118
Freudling, W., Romaniello, M., Bramich, D. M., et al. 2013, A&A, 559, A96
Gall, C., Hjorth, J., Watson, D., et al. 2014, Natur, 511, 326
Immler, S., Milne, P., & Pooley, D. 2010, ATel, 3012, 1
Kilic, M., Brown, W. R., Kenyon, S. J., et al. 2011, MNRAS, 413, L101
Lucy, L. B., Danziger, I. J., Gouiffes, C., & Bouchet, P. 1989, in IAU Coll. 120, Structure and Dynamics of the Interstellar Medium, 350 (Berlin: Springer), 164
Maeda, K., Nozawa, T., Sahu, D. K., et al. 2013, ApJ, 776, 5
Matsuura, M., Indebetouw, R., Woosley, S., et al. 2017, MNRAS, 469, 3347
Moriya, T. J., Maeda, K., Taddia, F., et al. 2013, MNRAS, 435, 1520
Newton, J., & Puckett, T. 2010, CBET, 2532, 1
Ofek, E. O., Zackay, B., Gal-Yam, A., et al. 2019, PASP, 131, 054204
Ofek, E. O., Zoglauer, A., Boggs, S. E., et al. 2014, ApJ, 781, 42
Patat, F., Taubenberger, S., Benetti, S., Pastorello, A., & Harutyunyan, A. 2011, A&A, 527, L6
Pozzo, M., Meikle, W. P. S., Fassia, A., et al. 2004, MNRAS, 352, 457
Sarangi, A., Dwek, E., & Arendt, R. G. 2018, ApJ, 859, 66
Schlegel, D. J., Finkbeiner, D. P., & Davis, M. 1998, ApJ, 500, 525
Seitenzahl, I. R., Timmes, F. X., & Magkotsios, G. 2014, ApJ, 792, 10
Smith, N. 2017, Interacting Supernovae: Types IIn and Ibn (Cham: Springer), 403
Smith, N., Li, W., Miller, A. A., et al. 2011, ApJ, 732, 63
Smith, N., Silverman, J. M., Chornock, R., et al. 2009, ApJ, 695, 1334
Smith, N., Silverman, J. M., Filippenko, A. V., et al. 2012, AJ, 143, 17
Stoll, R., Prieto, J. L., Stanek, K. Z., et al. 2011, ApJ, 730, 34
Stritzinger, M., Taddia, F., Fransson, C., et al. 2012, ApJ, 756, 173
Sugerman, B. E. K., Ercolano, B., Barlow, M. J., et al. 2006, Sci, 313, 196
Szalai, T., Zsíros, S., Fox, O. D., Pejcha, O., & Müller, T. 2019, ApJS, 241, 38
Tody, D. 1986, Proc. SPIE, 627, 733
Tody, D. 1993, in ASP Conf. Ser. 52, IRAF in the Nineties, ed. R. J Hanisch, R. J. V. Brissenden, & J. Barnes (San Francisco, CA: ASP), 173
Welch, D. L., Clayton, G. C., Campbell, A., et al. 2007, ApJ, 669, 525
Wesson, R., Barlow, M. J., Matsuura, M., & Ercolano, B. 2015, MNRAS, 446, 2089
Williams, B. J., & Fox, O. D. 2015, ApJL, 808, L22
Wooden, D. H., Rank, D. M., Bregman, J. D., et al. 1993, ApJS, 88, 477
Yamanaka, M., Okushima, T., Arai, A., Sasada, M., & Sato, H. 2010, CBET, 2539, 1
Zubko, V. G., Mennella, V., Colangeli, L., & Bussoletti, E. 1996, MNRAS, 282, 1321